Japan Sea Thermohaline Structure and Circulation. Part III: Autocorrelation Functions

PETER C. CHU

Naval Ocean Analysis and Prediction Laboratory, Department of Oceanography, Naval Postgraduate School, Monterey, California

WANG GUIHUA

Laboratory of Ocean Dynamic Processes and Satellite Oceanography, Second Institute of Oceanography, State Oceanic Administration, Hangzhou, China

YUCHUN CHEN

Cold and Arid Regions Environmental and Engineering, Research Institute, Lanzhou, China

(Manuscript received 29 January 2001, in final form 17 June 2002)

ABSTRACT

The autocorrelation functions of temperature and salinity in the three basins (Ulleung, Japan, and Yamato Basins) of the Japan/East Sea are computed using the U.S. Navy's Master Oceanographic Observational Dataset for 1930–97. After quality control the dataset consists of 93 810 temperature and 50 349 salinity profiles. The decorrelation scales of both temperature and salinity were obtained through fitting the autocorrelation function into the Gaussian function. The signal-to-noise ratios of temperature and salinity for the three basins are usually larger than 2. The signal-to-noise ratio of temperature is greater in summer than in winter. There is more noise in salinity than in temperature. This might be caused by fewer salinity than temperature observations. The autocorrelation functions of temperature for the three basins have evident seasonal variability at the surface: less spatial variability in the summer than in the winter. The temporal (spatial) decorrelation scale is shorter (longer) in the summer than in the winter. Such a strong seasonal variability at the surface may be caused by the seasonal variability of the net surface heat flux. The autocorrelation functions of salinity have weaker seasonal variability than those of the temperature field. The temporal and horizontal decorrelation scales obtained in this study are useful for designing an optimal observational network.

1. Introduction

The Japan/East Sea, hereafter referred to as JES, is a semienclosed ocean basin covering an area of 10^6 km^2 and is overlain by a pronounced monsoon surface wind. Its maximum depth exceeds 3700 m. It is isolated from the open ocean except for small (narrow and shallow) straits that connect the JES with the North Pacific (Korea/Tsushima and Tsugaru Straits) and with the Okhotsk Sea (Soya and Tatar Straits) (Fig. 1). The JES contains three major basins called the Japan Basin (JB), Ulleung Basin (UB), and Yamato Basin (YB), and has a high central plateau called the Yamato Rise (YR). The JES's basinwide circulation pattern, boundary currents, Subpolar Front (SPF), mesoscale eddy activities, and deep-water formation are similar to those in a larger ocean.

Seasonal variability of the JES thermohaline structure has been studied based on limited datasets (Isoda and Saitoh 1988, 1993; Kano 1980; Maizuru Marine Observatory 1997) and on a complete historical dataset (Chu et al. 2001b). Although the seasonal thermal variability at depth 150 m is weaker than at the surface, the SPF still occurs all the time throughout the year and is located at almost the same location as at the surface. It divides the water masses with different characteristics. North of the SPF, temperature is low (1°–3°C) and vertically uniform for the whole water column throughout the year. South of the SPF, temperature is stratified and changes from 5° to 9°C. The SPF meandering at 131°, 134°, and 138°E forms several mesoscale eddies (Chu et al. 2001b). The SPF meandering near Okin Gunto (134°E) in spring was previously reported by Isoda and Saitoh (1988, 1993).

Miyazaki (1953) found a low salinity layer in the SPF region, which Kim and Chung (1984) called the JES Intermediate Water (JIW). After analyzing the comprehensive hydrographic data for the whole JES collected by the Japan Meteorological Agency, the Maizuru Marine Observatory, and the Hydrographic Department of

Corresponding author address: Dr. Peter C. Chu, Department of Oceanography, Naval Postgraduate School, Monterey, CA 93943.
E-mail: chu@nps.navy.mil

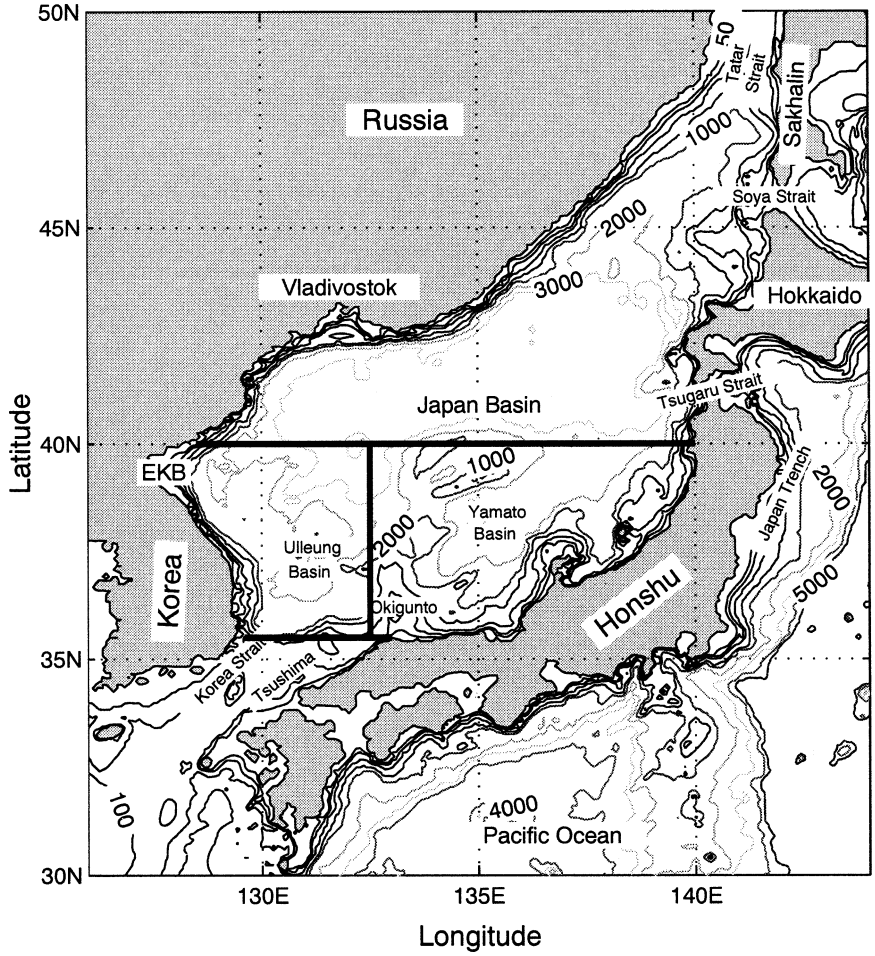

FIG. 1. Geography and isobaths showing the bottom topography of the Japan/East Sea (JES). Nonuniform contour intervals are used.

the Japan Maritime Safety Agency, Senjyu (1999) shows the existence of a salinity minimum (SMIN) layer (i.e., JIW) between the surface water and the JES ''Proper Water.''

With the hydrographic data collected from an international program, Circulation Research of the East Asian Marginal Seas (CREAMS) 1993–96, Kim and Kim (1999) found high salinity water with high oxygen in the eastern JB (i.e., north of SPF) which they called the ''High Salinity Intermediate Water'' (HSIW). Kim et al. (1999) found that the upper warm water is most saline in the UB and YB, that salinity of the intermediate water is the highest in the eastern JB, and that the deep cold water has highest salinity in the JB. This indicates that the three basins have different thermohaline structures.

In the first two parts of this paper, Chu et al. (2001a,b) reported the seasonal variation of the thermohaline structure and calculated currents from the navy's unclassified Generalized Digital Environmental Model (GDEM; Teague et al. 1990) temperature and salinity data on a $10' \times 10'$ grid. The GDEM for the JES is built on historical profiles. A three-dimensional estimate of the absolute geostrophic velocity field was obtained from the GDEM temperature and salinity fields using the P-vector method (Chu 1995). The climatological mean and seasonal variabilities of the thermohaline structure and the calculated currents such as the SPF, the Tsushima Warm Current (TWC), and its bifurcation were identified.

The thermohaline variabilities of these basins can be determined through computing the autocorrelation functions (ACF) of temperature and salinity at depth (z) using historical data. The ACF for temperature or salinity is given by (Chu et al. 1997b)

$$\eta(l, z) = \frac{1}{s^2} \int^{L} \psi'(l_0, z)\psi'(l_0 + l, z)\, dl_0, \qquad (1)$$

where ψ' is the anomaly (relative to the climatological mean values), l_0 denotes the independent space/time vectors defining the location of points in a sampling space L, l is the space/time lag, and s^2 the variance; η is computed by paring the anomalies into bins depend-

ing upon their separation in space/time, *l*. The values of η are obtained from calculating the correlation coefficient for all the anomaly pairs in each bin constructed for the combination of different lags.

Temporal and horizontal decorrelation scales of the JES thermohaline fields have not been calculated before. The U.S. Navy's Master Oceanographic Observational Data Set (MOODS) contains (93 810) temperature and (50 349) salinity profiles (unclassified) for JES during 1930–97 (Fig. 2). This provides the opportunity to compute the thermohaline ACFs.

The outline of this paper is as follows: Section 2 is background on the JES current systems and the division of data on the basis of the hydrographic properties. Section 3 discusses the irregularity of the navy's MOODS data. Sections 4 and 5 depict space/time sorting and ACF calculation. The seasonal variabilities of the decorrelation scales and their application are discussed in sections 6 and 7. In section 8 we present our conclusions.

2. JES current systems and geographic regions

The JES has subtropical and subpolar circulations separated by SPF. Most of the nearly homogeneous water in the deep part of the basin is called the ''Japan Sea Proper Water'' (Moriyasu 1972) and is of low temperature and low salinity. Above the Proper Water, the TWC, dominating the surface layer, flows in from the East China Sea through the Korea/Tsushima Strait and carries warm, salty Kuroshio water from the south. The Liman Cold Current (LC) carries cold fresh surface water from the north and northeast. The properties of this surface water are generally believed to be determined by the strong wintertime cooling coupled with freshwater input from the Amur River and the melting sea ice in Tatar Strait (Martin and Kawase 1998). The LC flows southward along the Russian coast, beginning at a latitude slightly north of Soya Strait, terminating off Vladivostok, and becoming the North Korean Cold Current (NKCC) after reaching the North Korean coast (Yoon 1982).

The TWC separates into two branches, which flow through the western and eastern channels of the Korea/Tsushima Strait (Kawabe 1982a,b; Hase et al. 1999). The flow through the eastern channel closely follows the Japanese coast and is called the ''Nearshore Branch'' (Yoon 1982) or the first branch of TWC (FBTWC: Hase et al. 1999). The flow through the western channel is called the East Korean Warm Current (EKWC), which closely follows the Korean coast until it separates near 37°N into two subbranches. The western subbranch moves northward and forms a cyclonic eddy over UB off the eastern Korean coast. The eastern subbranch flows eastward to the western coast of Hokkaido Island, and becomes the second branch of the TWC (SBTWC; Hong and Cho 1983). However, the SBTWC may not exist all year and cannot always be found around the shelf because its path is influenced by the development of eddies (Hase et al. 1999).

The NKCC meets the EKWC at about 38°N. After separation from the coast, the NKCC and the EKWC converge and form a strong front that stretches in the zonal direction across the basin. The NKCC makes a cyclonic recirculation gyre in the north but most of the EKWC flows out through Tsugaru and Soya Straits (Uda 1934). The formation of NKCC and separation of EKWC are due to local forcing by wind and buoyancy flux (Seung 1994). Large meanders develop along the front and are associated with warm and cool eddies.

The ACF depends on water mass properties. Different thermohaline characteristics are found north and south of the SPF, which is located about 40°N. The upper warm water is more saline south of the SPF, while the intermediate and deep cold water is more saline north of the SPF (Kim et al. 1999). South of the SPF, different thermohaline characteristics are found west and east of 132°E. The southwestern JES west of 132°E is the upstream region of the JIW (Senjyu 1999). The lowest salinity and the highest oxygen concentration are found in the 38°–40°N areas west of 132°E. The JIW takes two flow paths: an eastward flow along the SPF and a southward flow parallel with the Korean coast in the region west of 132°E. The circulation pattern west and east of 132°E is also different: dual eddies (cyclone in the north and anticyclone in the south) occur west of 132°E, while there are two branches of TWC east of 132°E (Senjyu 1999). Thus, 40°N latitude and 132°E longitude are used here to divide the JES into three parts (Fig. 1) with different water mass characteristics.

The Korean/Tsushima Strait is a major continental shelf with many observations. However, the water mass on the shelf, largely affected by the atmospheric forcing, is different from the water mass of the JES basin and therefore should be deleted for the computation. Two approaches are used: (i) a southern boundary is set up at 35.5°N and (ii) profiles in water depth shallower than 100 m are excluded.

Thus, the ACF is separately computed for the three parts of JES: north of 40°N (represented by JB), west of 132°E between 35.5° and 40°N (represented by UB), and east of 132°E between 35.5° and 40°N (represented by YB). The partition into JB, UB, and YB here is based on water mass characteristics and may not be exactly the same as the geographic definitions.

3. Irregularity of the MOODS

To investigate the seasonal variation of the temporal and spatial scales for the three basins, the MOODS was binned into four seasons. The seasons were defined according to the convention of the Naval Oceanographic Office for the JES: January–March constitute winter; April–June, spring; July–September, summer; and October–December, fall.

The main limitation of the dataset is its irregular dis-

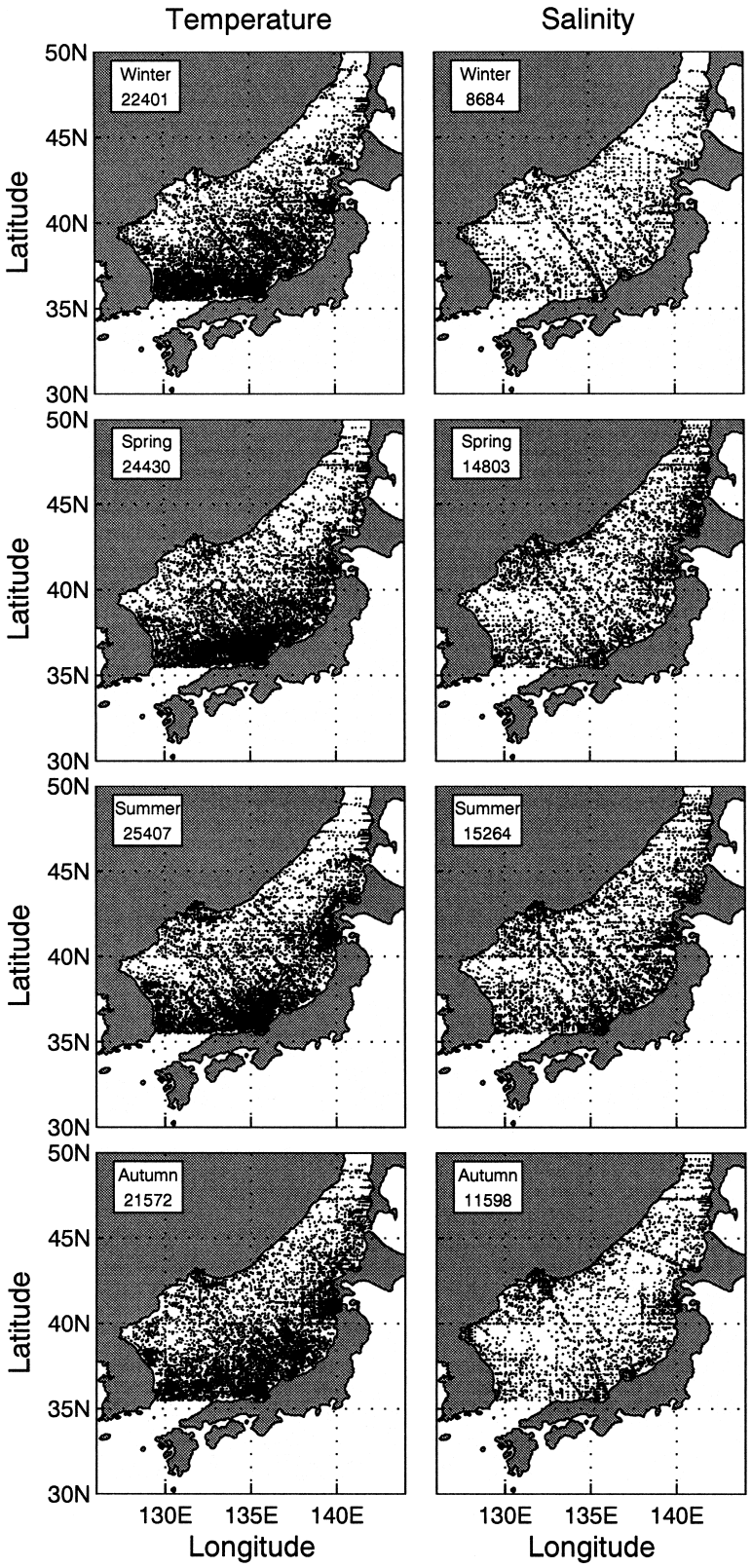

FIG. 2. MOODS stations from 1930 to 1997: (a) temperature and (b) salinity.

TABLE 1. Number of temperature profiles in the database for each basin and each season.

	JB	UB	YB
Winter	5203	4612	12 586
Spring	7704	4160	12 566
Summer	8163	4739	12 505
Fall	7012	4503	10 057

tribution in time and space. Certain periods and areas are oversampled while others lack enough observations to gain any meaningful insights (Chu et al. 1997a). The vertical extent of the observations and data quality are also highly variable. The eastern coastal region of North Korea is a data sparse area. Horizontal (Fig. 2) and temporal irregularities along with the lack of data in certain regions must be carefully weighted in order to avoid statistically induced variability. Analysis was done on a mean seasonal basis using the data for all years.

The number of temperature and salinity (Fig. 2) observations differs drastically from basin to basin (Tables 1 and 2). The YB has the most temperature observations in the four seasons. However, JB has the most salinity observations in spring and summer. Salinity profiles are fewer than temperature profiles in all seasons and for all basins. The number of observations vary with depth (Fig. 3). Many temperature and salinity samples were collected above depth 100 m. The vertical variation of sampling changes from basin to basin. For example, in UB, the number of *T, S* samples decreases rapidly with depth below 75 m. In JB, the number of temperature samples reaches a maximum at depth 200–250 m in spring and summer.

4. ACF computation

The three basins (JB, UB, YB) may be treated as quasi-isolated systems. Therefore, it is assumed that the ACF for each basin depends only on the distance between two locations in order to reduce the number of bins. Without this assumption, the number of bins is very large—for example, 27 000 if each of the temporal and spatial (x and y) lags has 30 bins.

For each observation $\psi_o^{(z)}$ at depth z (ψ represents T, S), the closest grid point climatological value (from GDEM) $\overline{\psi}_l^{(z)}$ is found and the anomaly, $\psi_o^{(z)\prime} = \psi_o^{(z)} - \overline{\psi}_l^{(z)}$ is computed. GDEM is the navy's global climatological monthly mean temperature and salinity dataset ($0.5° \times 0.5°$) from the surface to bottom. The current version of the GDEM climatology was based on the navy's MOODS (Teague et al. 1991).

The ACF is calculated (see appendix A) for each spatial lag bin (with increment $\Delta r = 10$ km) and temporal lag bin (with increment $\Delta t = 1$ day). For each individual anomaly, $\psi_o^{(z)\prime}$, all the other data points, $\hat{\psi}_o^{(z)\prime}$ are sorted into different spatial and temporal bins within the four seasons. If the lags between $\psi_o^{(z)\prime}$ and $\hat{\psi}_o^{(z)\prime}$ (called a data pair) are within Δr_0 (5 km) and Δt_0 (0.5 day), the corresponding pair is placed into bin (0, 0). If the horizontal lag is between $m\Delta r - \Delta r_0$ and $m\Delta r + \Delta r_0$, and the temporal lag between $n\Delta t - \Delta t_0$ and $n\Delta t + \Delta t_0$, the pair is placed into the bin (m, n).

The pair–number distributions, $P(m, n)$, of temperature and salinity for winter and summer are illustrated in Figs. 4 and 5. We see uneven distribution in the temporal and spatial bins, however, the seasonal variation of $P(m, n)$ is weaker than the vertical variation. The ACF is not computed if the number of pairs is less than 200 in most bins.

Taking the YB as an example, $P(m, n)$ of surface temperature is greater than 2000 in most bins in winter (Fig. 4a) and summer (Fig. 5a). The maximum $P(m, n)$ is located in bins near temporal lags 1–2 day and spatial lags 80–120 km for temperature (Figs. 4a and 5a), and 1–2 day and 20–80 km for salinity (Figs. 4b and 5b); $P(m, n)$ usually decreases with depth. Its values at depth 300 m are about half of those at the surface. Furthermore, in UB below 100 m, $P(m, n)$ is too small (200 in most bins) to perform the ACF computation.

5. ACFs of the JES thermohaline fields

a. Temperature

The spatial dependence of ACF temperature, $\eta^{(z)}(\tau, r)$, is obtained at several different temporal lags: $\tau = 0$ (''no lag''), 5, and 15 days. The ACFs are plotted for different seasons and five depths ($z = 0$, 50, 100, 200, and 300 m) in order to see the seasonal and vertical variations (Fig. 6). The depths are divided into three groups: surface (0 m), subsurface (50–200 m), and deep (300 m and below). A given depth is used only if the number of observations at that depth is greater than 3000.

The ACF temperature for the three basins has the following features: 1) Its values are larger with no temporal lag (solid curves in Fig. 6) than with temporal lags (dotted and dashed–dotted curves in Fig. 6); 2) It decreases with the spatial lag r for all seasons and for all depths except in UB, where it increases with r when $r > 150$ km; 3) At the surface, the decrease of the ACF with spatial lag r is moderate, indicating less spatial variability; and 4) The ACF decreases faster with spatial lag r in the subsurface layers for all seasons.

1) JAPAN BASIN

The number of temperature observations is greater than 4000 from the surface to depth 300 m and much less than 4000 below 300 m (Fig. 3a). Thus, it is reasonable to present the ACF temperature from the surface to 300 m. The ACF temperature (Fig. 6) has the following features.

(i) *Seasonal variability at the surface.* At the surface, decrease of ACF temperature with the spatial lag r is slower in the summer than in the winter. For example,

TABLE 2. Number of salinity profiles in the database for each basin and each season.

	JB	UB	YB
Winter	2551	2706	3427
Spring	5459	4212	5132
Summer	5718	4098	5448
Fall	3820	3836	3942

$\eta^{(0)}(0, r)$ decreases from 0.95 ($r = 0$) to 0.78 ($r = 200$ km) in the summer (only 0.17 reduction), and from 0.9 ($r = 0$) to 0.10 ($r = 200$ km) in the winter (0.8 reduction). This indicates that SST has less spatial variability in the summer than in the winter.

(ii) *Weak vertical variability from the surface to the subsurface in the winter*. The ACF temperature varies slightly from the surface to 200-m depth (Fig. 6a), indicating a relatively uniform thermal structure in vertical. However, in the summer, the ACF temperature changes drastically from the surface from the subsurface (50–200-m depth; Fig. 6b).

(iii) *High spatial coherence in the deep layer*. For both summer and winter, $\eta^{(0)}(0, r)$ at 300 m is greater than 0.4 for all r and is usually larger than that at the other depths except at the surface in the summer. This indicates that the spatial coherence is higher at 300 m than at the other depths. The high spatial coherence in the deep layer is consistent with the concept of JES Proper Water proposed by Moriyasu (1972).

2) ULLEUNG BASIN

The number of temperature observations is greater than 3000 from the surface to 100-m depth, and much less than 3000 below 100-m depth (Fig. 3a). Thus, it is reasonable to present the ACF temperature from the surface to 100 m. The ACF temperature (Fig. 6) has the following features.

(i) *Seasonal variability at the surface.* At the surface, there is less spatial variability in the summer than in the winter. For example, $\eta^{(0)}(0, r)$ decreases from 0.95 ($r = 0$) to 0.47 ($r = 170$ km) in the summer (0.48 reduction), and decreases from 0.9 ($r = 0$) to nearly 0 ($r = 170$ km) in the winter (0.9 reduction).

(ii) *Less vertical variability from the surface to subsurface in the winter*. The ACF temperature varies slightly from the surface to 100-m depth (Fig. 6a), indicating a relatively uniform thermal structure in vertical. However, in the summer, the ACF temperature changes drastically from the surface to the subsurface (depth 50–100 m; Fig. 6b).

3) YAMATO BASIN

The number of temperature observations is greater than 4000 from the surface to 300-m depth, and much less than 4000 below 300-m depth (Fig. 3a). Thus, it is reasonable to present the ACF-temperature from the surface to 300 m. The ACF temperature (Fig. 6) has the following features.

(i) *Seasonal variability at the surface.* As in the JB and UB, there is less spatial variability in the summer than in the winter. For example, $\eta^{(0)}(0, r)$ is greater than 0.7 for all r in the summer, and decreases from 0.95 ($r = 0$) to 0.3 ($r = 200$ km) in the winter.

(ii) *Reduction of spatial coherence with depth.* Unlike in the JB, the ACF temperature generally decreases with depth, and does not reveal high values at 300-m depth. This reflects the greatest depth of the JES Proper Water in the YB than in the JB.

b. Salinity

The estimate of ACF salinity is not as good as the estimate of ACF temperature because the number of salinity observations is less than the number of temperature observations (cf. Fig. 3b to Fig. 3a). The spatial dependence of ACF salinity, $\eta^{(z)}(\tau, r)$ is obtained for 0, 5, and 15 day lags. The ACFs are plotted for different seasons and five depths ($z = 0$, 50, 100, 200, and 300 m; Fig. 7). The depth is picked up only if the number of observations at that depth larger than 2000. The ACF salinity for the three basins is similar to the ACF temperature.

1) JAPAN BASIN

The number of salinity observations is greater than 2000 from the surface to 100 m depth in the winter and to 300 m in the summer (Fig. 3b). Thus, it is reasonable to present the ACF salinity from the surface to 100 m (300 m) depth in the winter (summer).

(i) *Weak seasonal variability.* The seasonal variation of the ACF salinity (Fig. 7) is quite weak at all depths in comparison to the ACF temperature. There is no high spatial coherence in salinity at the surface in the summer. Decrease of ACF salinity with the spatial lag r is comparable between summer and winter at all depths. For example, $\eta^{(0)}(0, r)$ at the surface decreases from 0.90 ($r = 0$) to 0.18 ($r = 150$ km) in the summer (0.72 reduction), and decreases from 0.82 ($r = 0$) to 0.04 ($r = 150$ km) in the winter (0.78 reduction). This indicates that SST has comparable spatial variability in summer and winter.

(ii) *Weak vertical variability*. The ACF salinity varies slightly with depth (Fig. 7), indicating a relatively uniform haline structure in the vertical.

(iii) *High spatial coherence at deep layer*. Due to the data sparseness, the ACF salinity estimate at 300-m depth may be representative only in the summer (Fig. 7b). Its values at 300-m depth are greater than 0.4 for $r < 220$ km, indicating high spatial coherence. This feature is similar to the ACF temperature in JB.

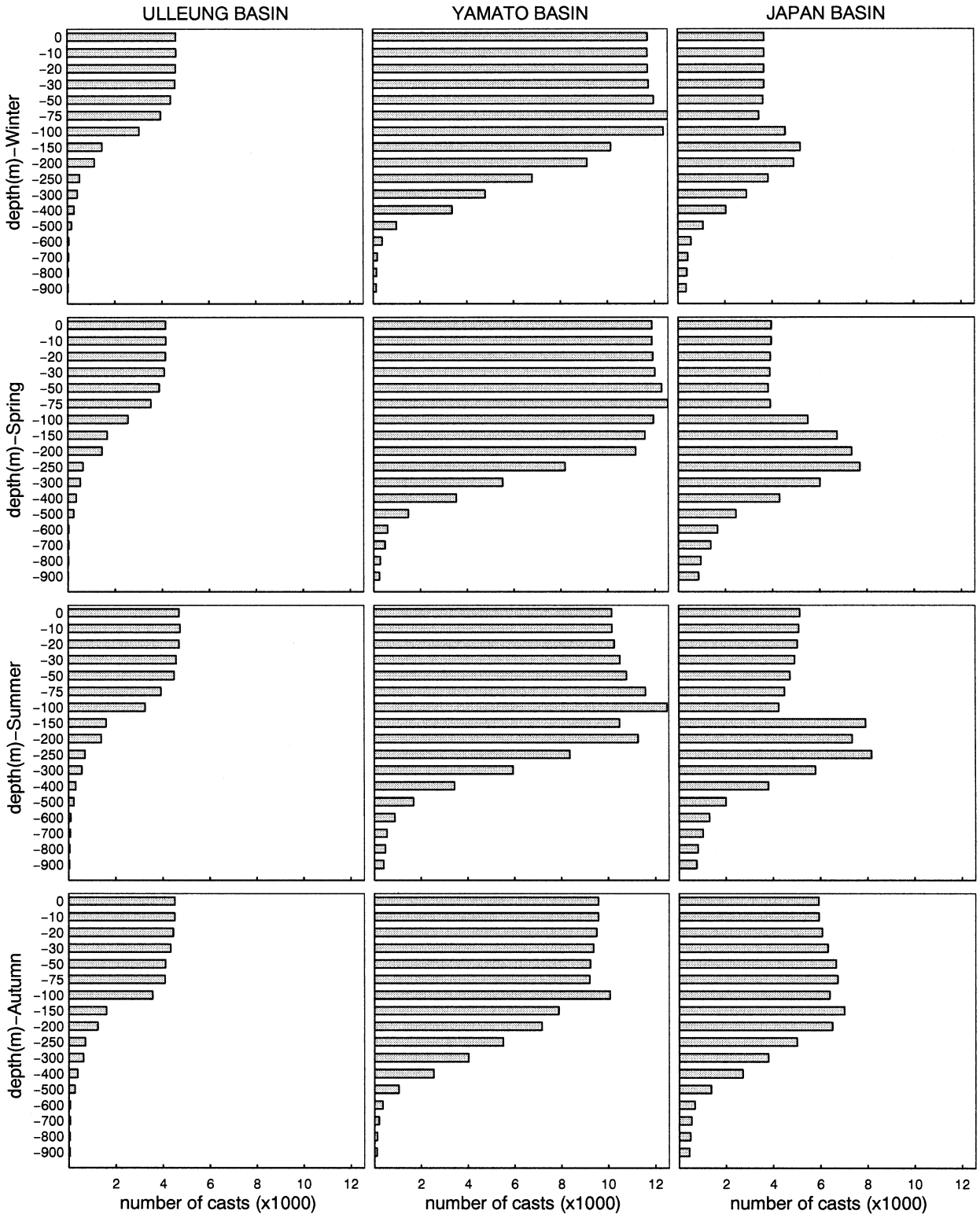

FIG. 3. Depth dependence of number of observations for (a) temperature and (b) salinity.

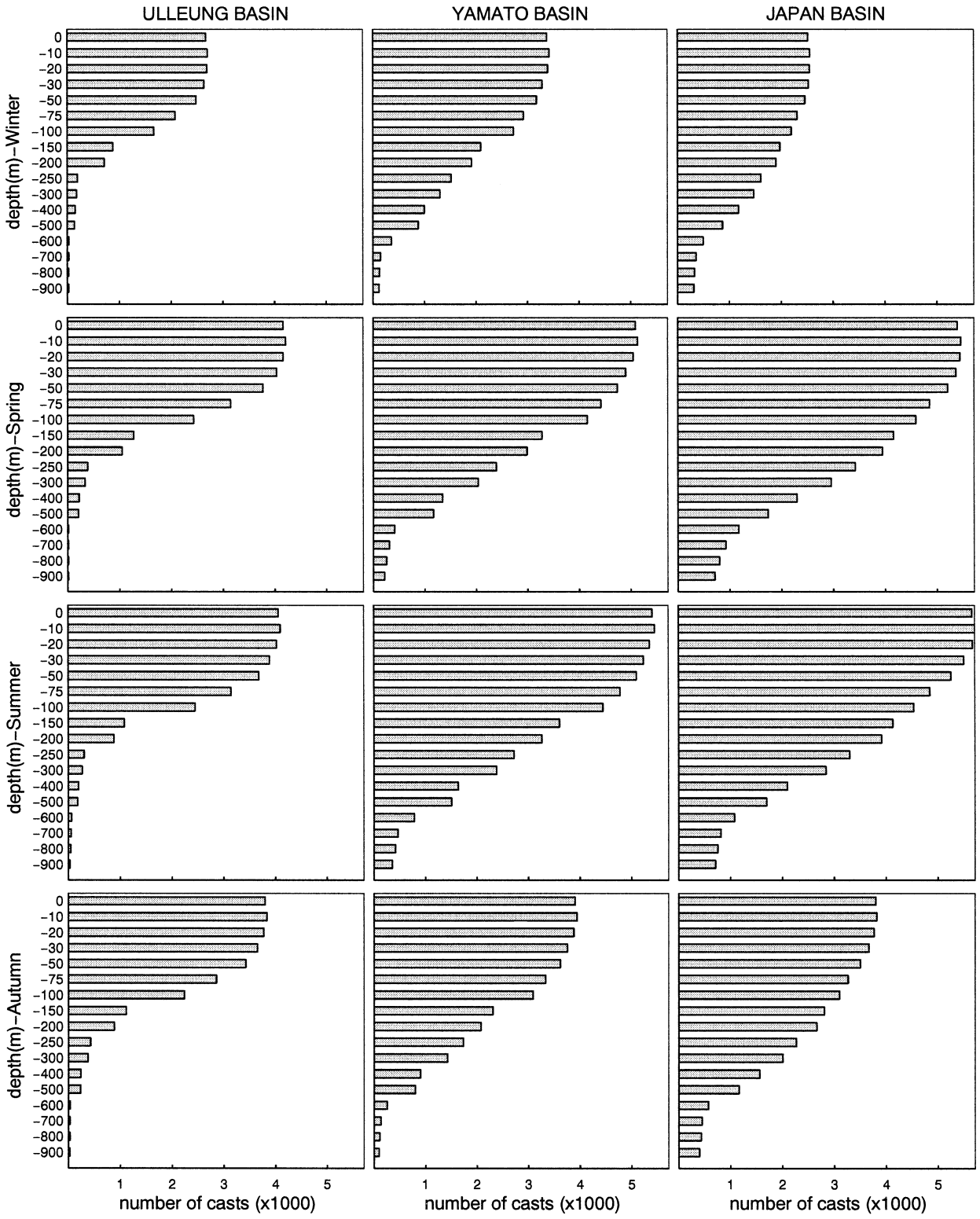

FIG. 3. (*Continued*)

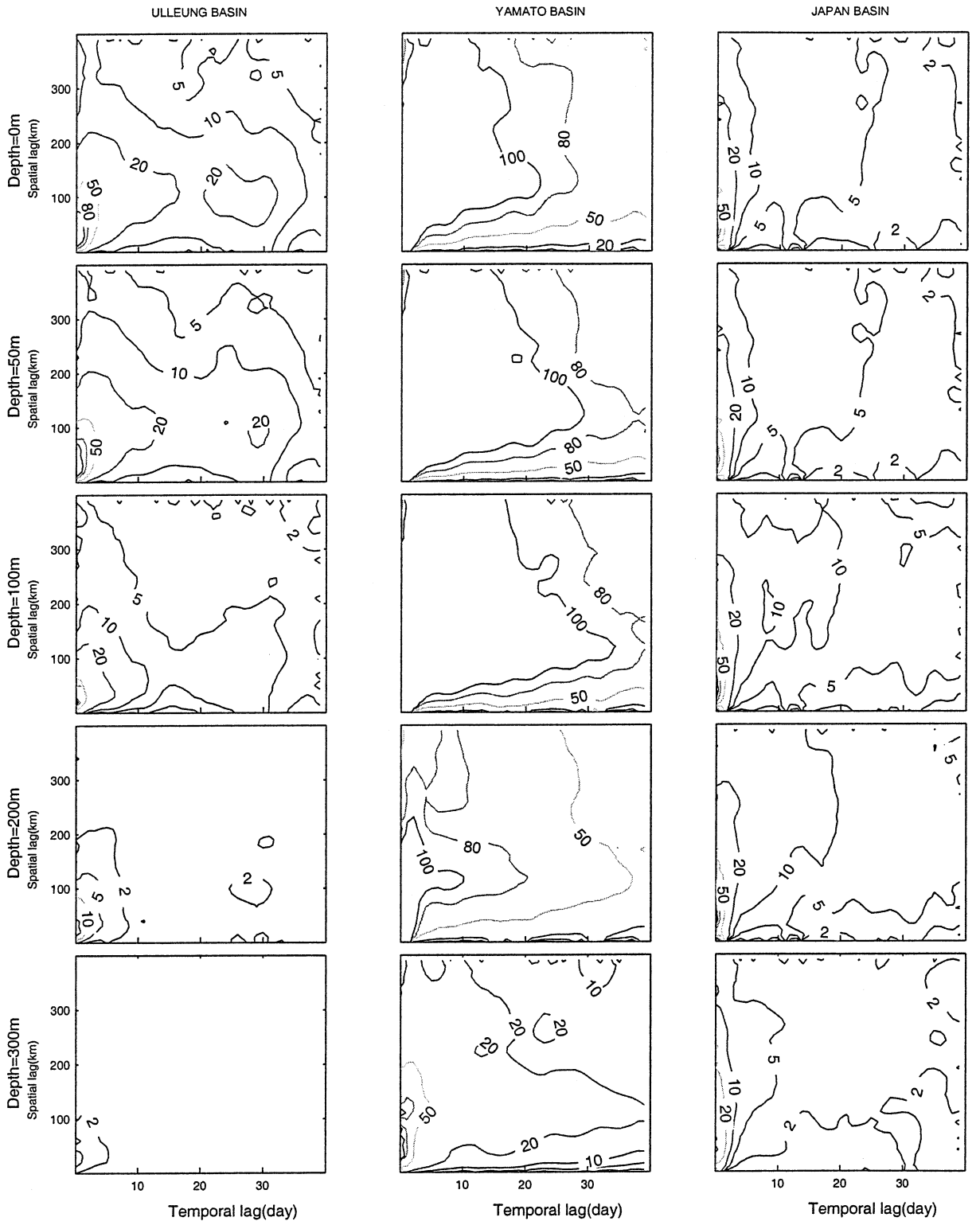

FIG. 4. The pair–number (in multiples of 100) distribution of temperature in the temporal and spatial lag bins for the three basins for (a) winter and (b) summer.

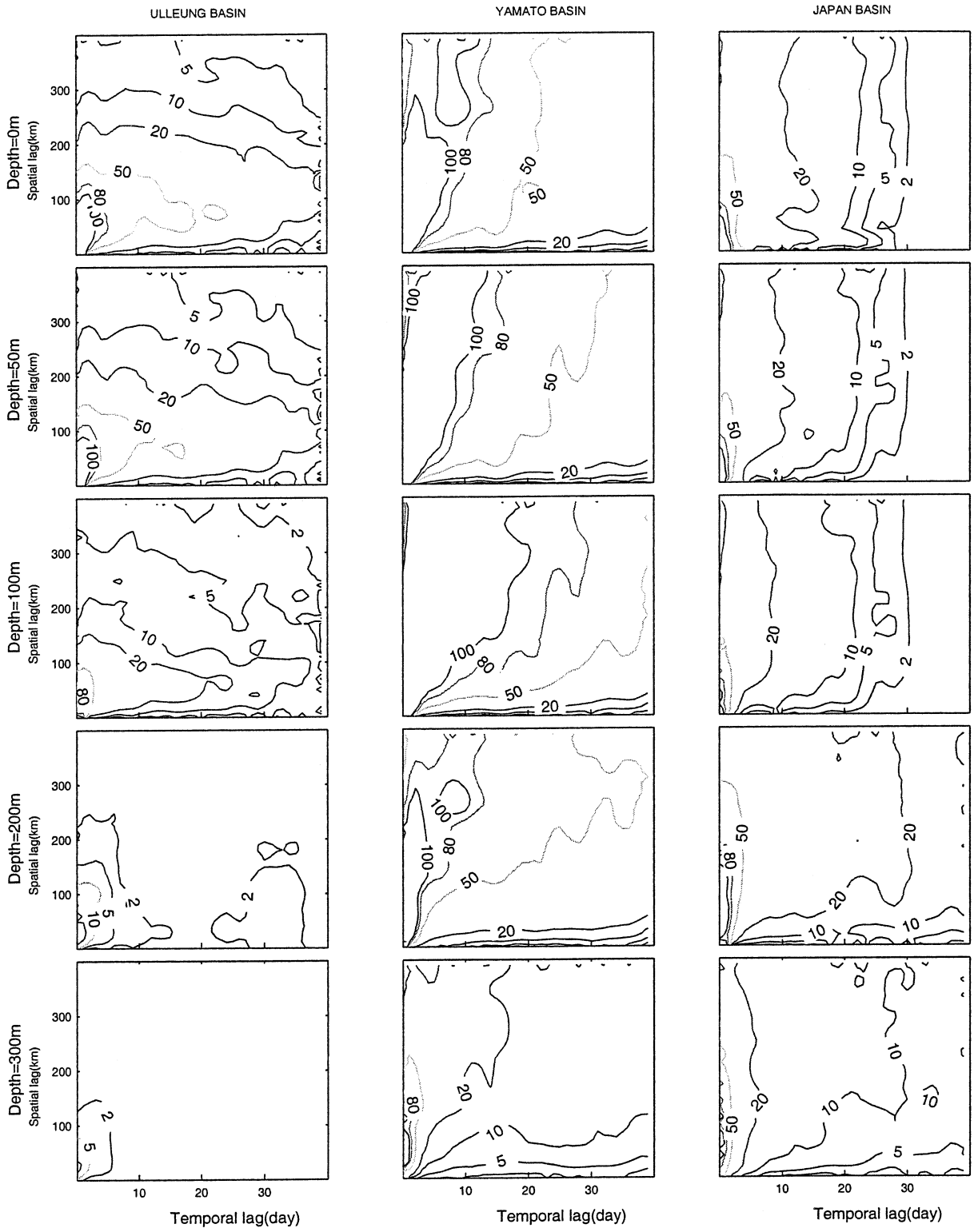

FIG. 4. (*Continued*)

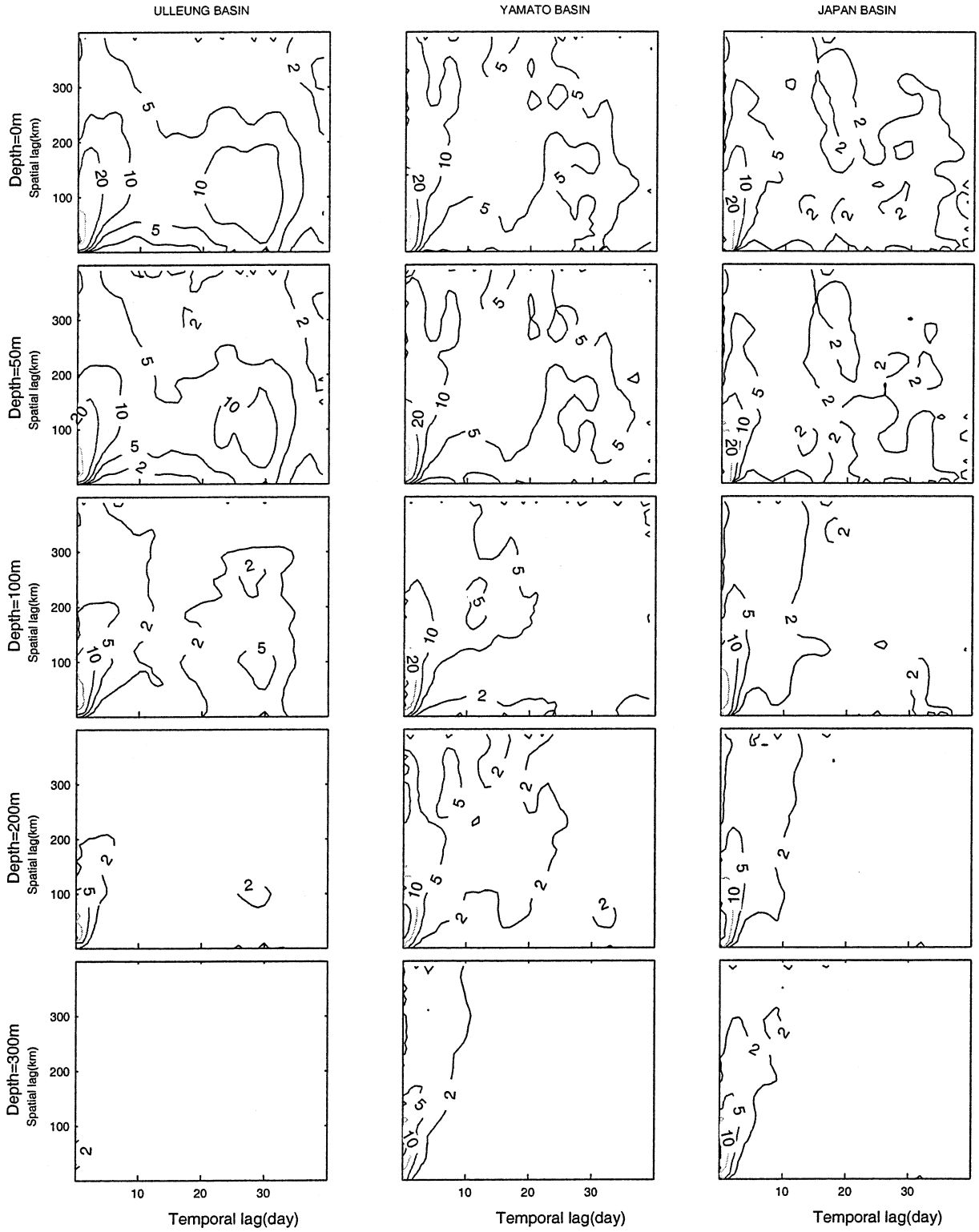

FIG. 5. The pair–number (in multiples of 100) distribution of salinity in the temporal and spatial lag bins for the three basins for (a) winter and (b) summer.

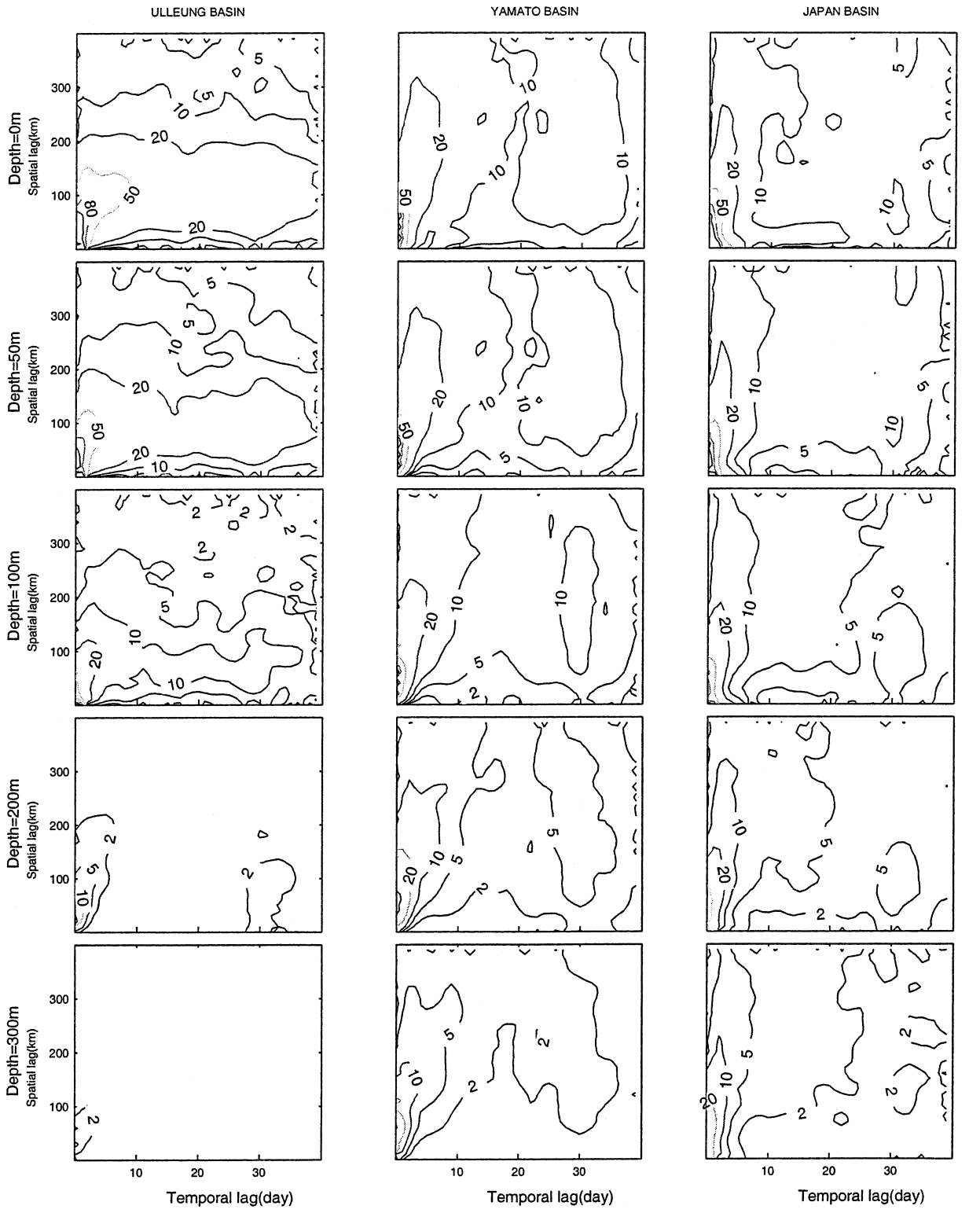

FIG. 5. (*Continued*)

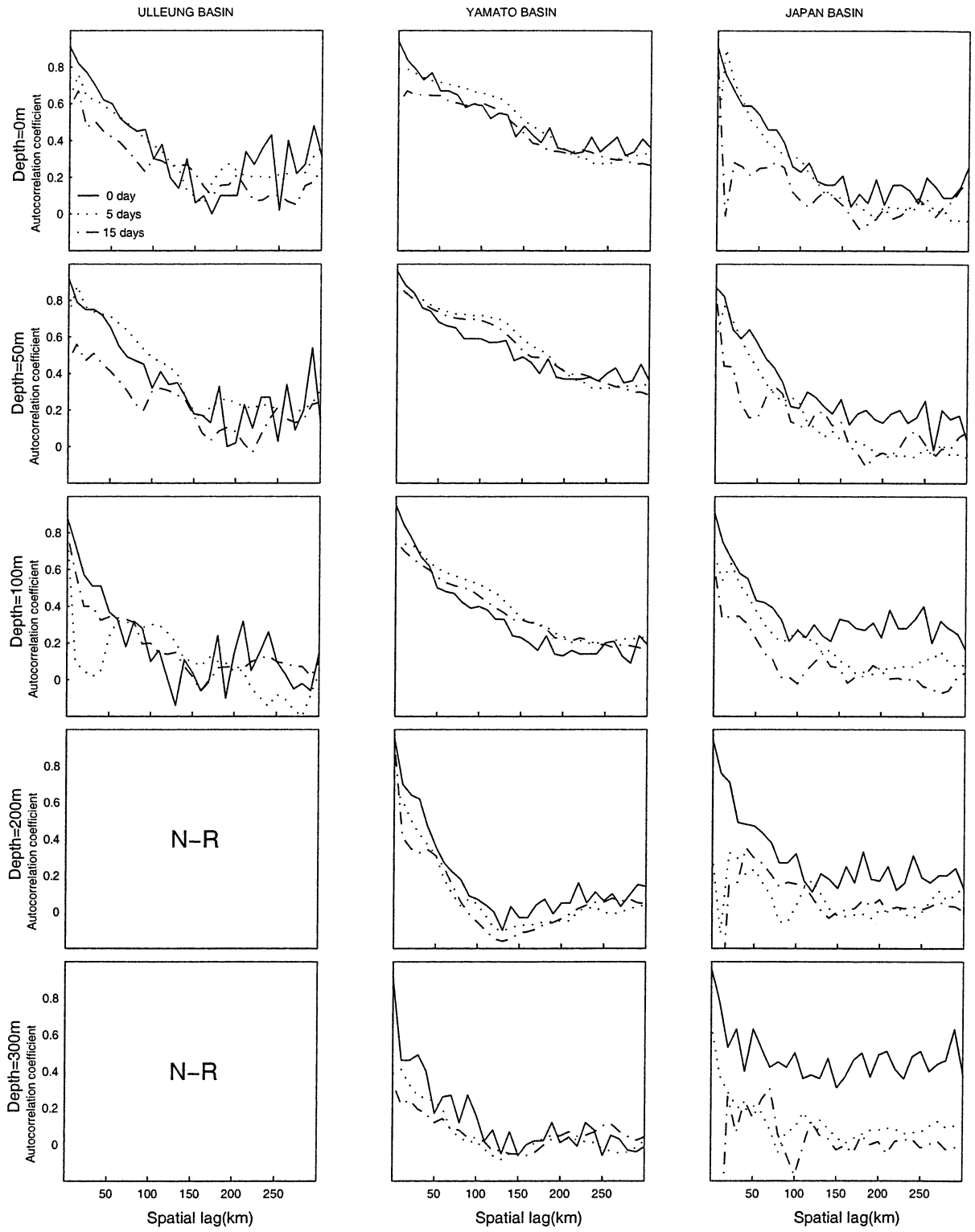

FIG. 6. Spatial variation of ACF temperature of the three basins at different temporal lags: $n = 0$ (no lag, solid curve), $n = 5$ (lag 5 day, dotted curve), and $n = 15$ (lag 15 day, dotted–dashed curve) for five different depths: (a) winter and (b) summer. The symbol N–R means nonrepresentative because of insufficient data.

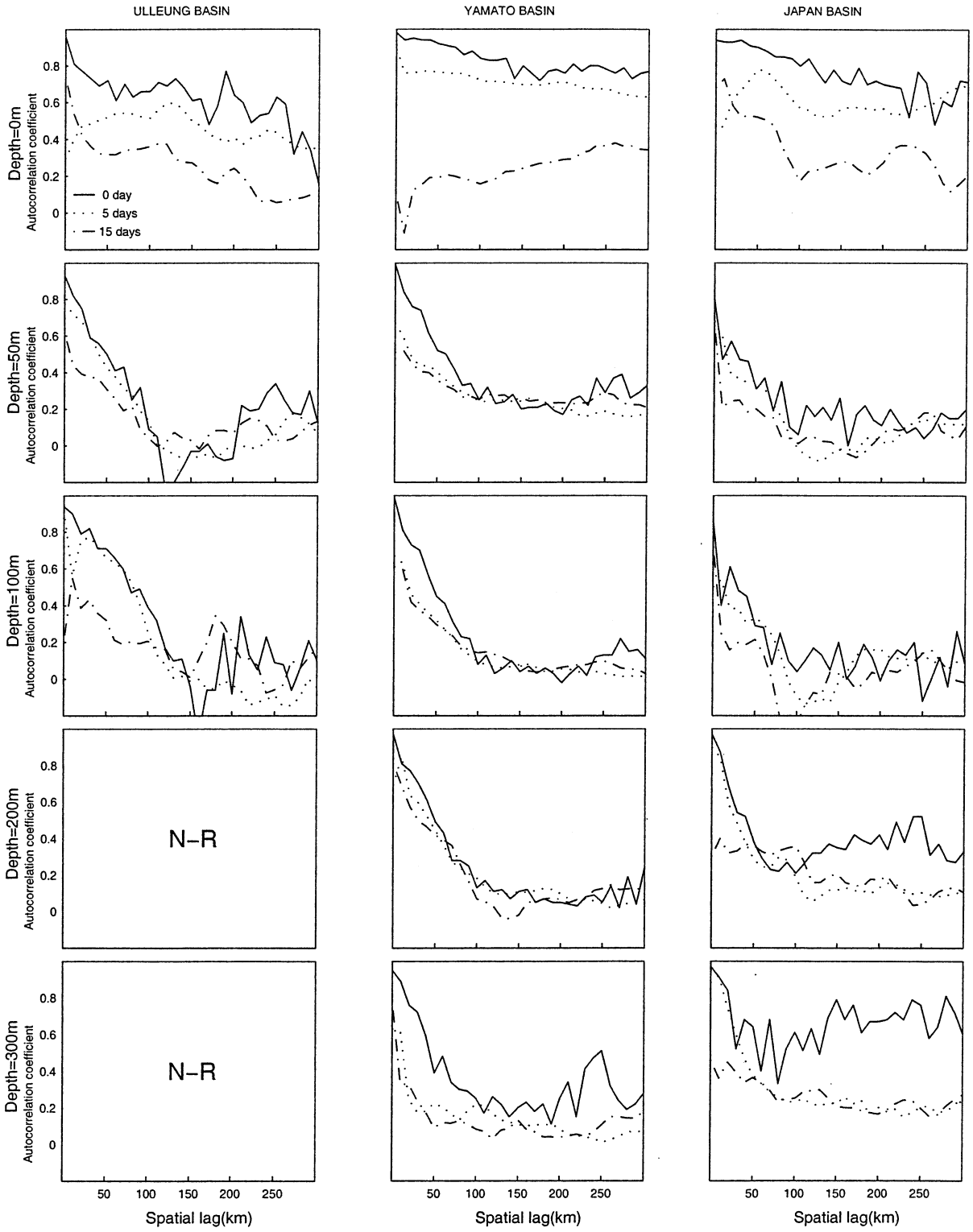

FIG. 6. (*Continued*)

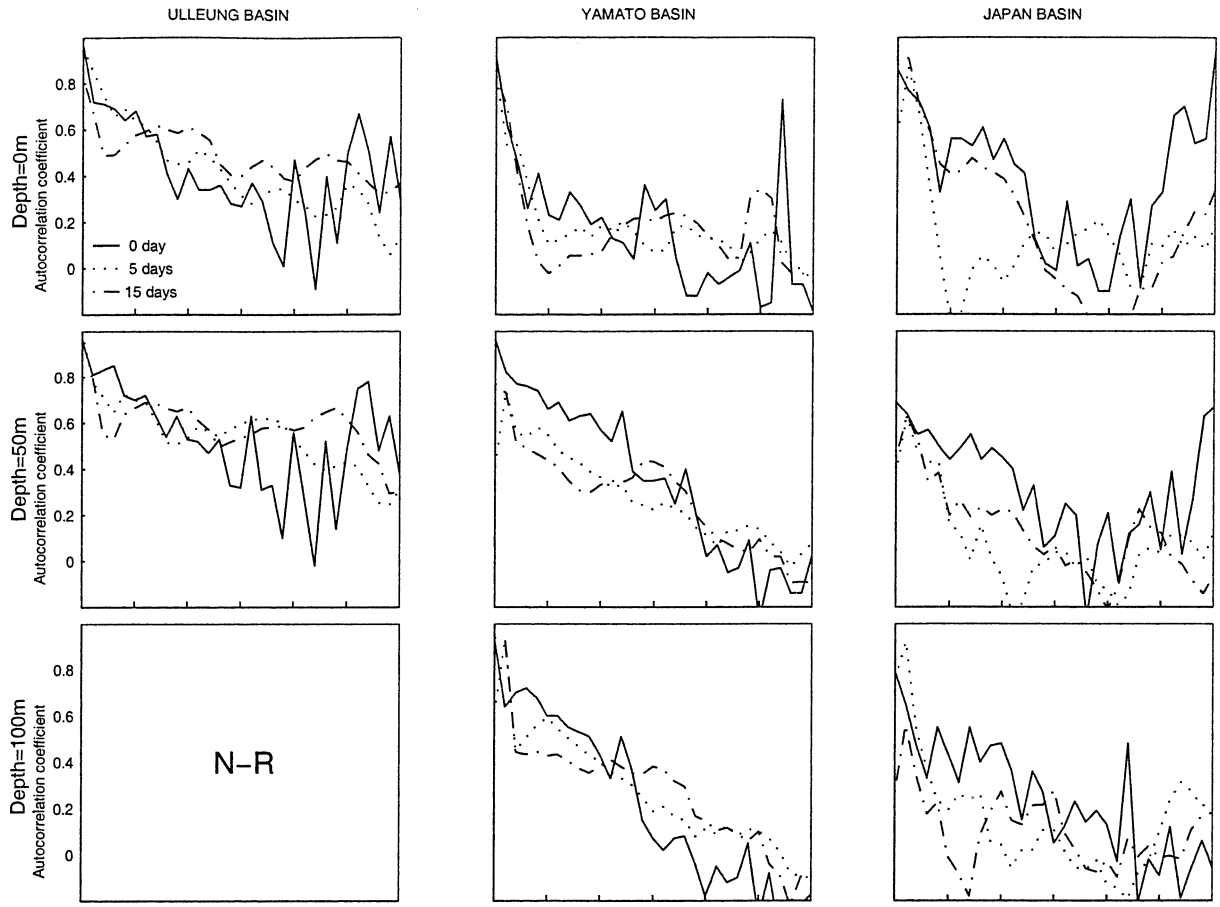

FIG. 7. Spatial variation of ACF salinity of the three basins at different temporal lags: $n = 0$ (no lag, solid curve), $n = 5$ (lag 5 day, dotted curve), and $n = 15$ (lag 15 day, dotted–dashed curve) for five different depths: (a) winter and (b) summer. The symbol N–R means nonrepresentative because of insufficient data.

2) ULLEUNG BASIN

The number of salinity observations is greater than 2000 from the surface to 50 m in the winter and to 100 m in the summer (Fig. 3b). Thus, it is reasonable to present the ACF salinity from the surface to 50 m (100 m) in the winter (summer). The ACF salinity (Fig. 7) in the UB has the following features.

(i) *Weak seasonal variability at the surface.* The seasonal variation of the ACF salinity (Fig. 7) is quite weak at the surface in comparison to the ACF temperature. There is no high spatial coherence in salinity at the surface in the summer. Decrease of ACF salinity with the spatial lag r is comparable between summer and winter at the surface, indicating that the surface salinity has comparable spatial variability between summer and winter.

(ii) *Subsurface seasonal variability*. The ACF salinity has evident seasonal variability at 50-m depth. Its values are generally higher in the winter than in the summer. For example, the no-lag ACF salinity, $\eta^{(0)}(0, r)$, varies from 0.97 ($r = 0$) to 0.57 ($r = 100$ km) in the winter, and changes from 0.60 ($r = 0$) to 0.08 ($r = 100$ km) in the summer. This indicates that the subsurface salinity has stronger spatial variability in the summer than in the winter.

3) YAMATO BASIN

The number of salinity observations is greater than 2000 from the surface to depth 100 m in the winter and to 200 m in the summer (Fig. 3b). Thus, it is reasonable to present the ACF salinity from the surface to 100 m (200 m) in the winter (summer). The ACF salinity (Fig. 7) in YB has the following features.

(i) *Seasonal variability at the surface.* Different from JB and UB, the surface ACF salinity in the YB has an evident seasonal variability with higher values in the summer than in the winter. For example, $\eta^{(0)}(0, r)$ is larger than 0.3 for all r in the summer, and for $r < 25$ km in the winter.

(ii) *High spatial coherence at depth 200 m in the summer*. The ACF salinity decreases with depth from the surface to depth 100 m, and then increases with depth from 100 to 200 m. The values at 200 m are evidently higher than at 50 m and 100 m.

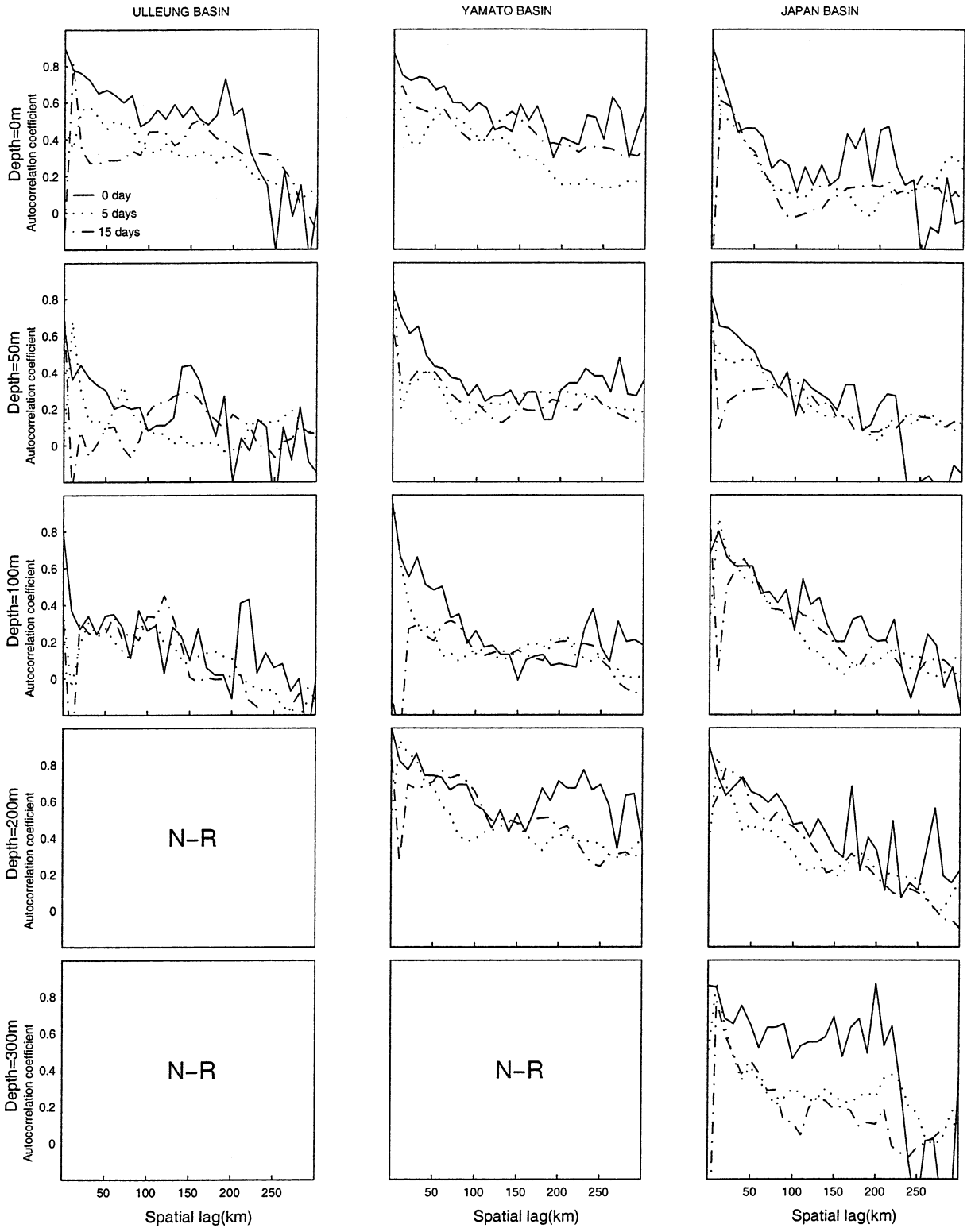

FIG. 7. (*Continued*)

TABLE 3. Seasonal and vertical variations of the Japan Basin temperature decorrelation scales.

Season	Depth (m)	Temporal (day)	Spatial (km)	SNR (λ)
Winter	Surface	23.0	242	3.18
	50	24.0	228	2.59
	100	26.2	220	3.18
	200	24.2	204	3.96
	300	26.4	222	4.90
Summer	Surface	16.0	464	3.96
	50	24.1	238	2.00
	100	27.5	223	2.48
	200	31.5	248	5.69
	300	36.2	292	5.69

TABLE 4. Seasonal and vertical variations of the Ulleung Basin temperature decorrelation scales.

Season	Depth (m)	Temporal (day)	Spatial (km)	SNR (λ)
Winter	Surface	23.8	251	3.18
	50	25.1	254	3.39
	100	27.4	211	2.71
Summer	Surface	18.1	307	4.90
	50	31.4	247	3.64
	100	28.6	213	3.96

6. Seasonal variabilities of the decorrelation scales

If the computed ACF is fitted to a theoretical function, the thermohaline variability can be simply represented by temporal and spatial decorrelation scales. The larger the decorrelation scale, the less the variability is.

a. Gaussian ACF model

Similar to the previous calculated Yellow Sea ACF (Chu et al. 1997b), the ACF is fit to the Gaussian function (Phoebus 1988; Clancy 1983):

$$\hat{\eta}^{(z)}(m, n) = \hat{\eta}^{(z)}(0, 0) \times \exp[-A_z^2(m\Delta r)^2 - C_z^2(n\Delta\tau)^2], \quad (2)$$

where $\hat{\eta}^{(z)}(m, n)$ denotes the Gaussian fit of the ACF value (at depth z) in the bin with the spatial separation $m\Delta r$ and the temporal separation $n\Delta\tau$. Δr and $\Delta\tau$ are increments for the space/time separation; A_z^{-1} and C_z^{-1} are horizontal and temporal decorrelation scales at depth z. The dominant space/time scales obtained from η are important not only in determining sampling density but also in the optimum interpolation of the observed data. We use the same F test depicted in Chu et al. (1997b) to check if the Gaussian model (2) is significant. After the significance test, we confirm that the Gaussian model is reasonable for the JES thermohaline ACF.

The computed ACFs of temperature and salinity for different seasons and depths are then fit to a Gaussian function of the form of (2) by the regression method, which leads to the spatial and temporal decorrelation scales, A_z^{-1} and C_z^{-1}, respectively.

b. Seasonal variabilities of the temperature decorrelation scales

1) CHARACTERISTICS

Tables 3–5 present the temperature decorrelation scales and signal to noise ratios (SNRs) for JB, UB, and YB (see appendix B). The SNRs for both winter and summer are comparable to the Yellow Sea waters (shallower than 80 m), which is between 1.88 and 3.0 (Chu et al. 1997b). The largest noise level (smallest SNR) occurs at depth 50 m in the JB during the summer (SNR = 2.00, Table 3). The SNR is usually greater in the summer than in the winter.

The temporal and spatial decorrelation scales of temperature field have evident seasonal variability, especially at the surface. The temporal (spatial) decorrelation scale is shorter (longer) in the summer than in the winter.

2) PHYSICAL MECHANISM FOR THE SEASONAL VARIABILITY

The strong seasonal variability of ACF temperature may be related to the seasonal variability of the surface fluxes. The Comprehensive Ocean and Atmosphere Data Set (COADS) shows that the net surface heat flux (downward positive) is inhomogeneous in the winter (from -275 W m^{-2} in the southeast JES to -150 W m^{-2} in the northwest JES), and is quite homogeneous in the summer (nearly 75 W m^{-2}) over the whole JES (Slutz et al. 1985). This leads to a more uniform SST field (Chu et al. 1998, 2001b) in the summer than in the winter. Thus, the surface spatial decorrelation scales are much larger in the summer than in the winter.

Surface temporal decorrelation scales are much shorter in summer than in winter. This is caused by the shallower surface thermal mixed layer in the summer (less thermal inertia) due to strong solar heating. Only the upper-layer water is affected in the summer by the atmospheric forcing rather than the entire water column as in the winter.

TABLE 5. Seasonal and vertical variations of the Yamato Basin temperature decorrelation scales.

Season	Depth (m)	Temporal (day)	Spatial (km)	SNR (λ)
Winter	Surface	30.5	309	3.96
	50	36.9	315	4.90
	100	36.2	262	4.36
	200	30.0	191	4.36
	300	24.5	192	3.18
Summer	Surface	14.7	963	7.00
	50	25.4	276	9.95
	100	29.0	187	9.95
	200	31.0	200	5.69
	300	30.3	324	4.36

TABLE 6. Seasonal and vertical variations of the Japan Basin salinity decorrelation scales. Asterisk indicates SNR values below 2.

Season	Depth (m)	Temporal (day)	Spatial (km)	SNR
Winter	Surface	36.4	197	2.48
	50	36.4	191	1.49*
	100	36.8	170	1.94*
	200	—	—	—
	300	—	—	—
Summer	Surface	25.6	173	3.00
	50	27.5	166	2.13
	100	36.1	181	1.46*
	200	30.8	185	3.00
	300	29.8	193	2.48

TABLE 7. Seasonal and vertical variations of the Ulleung Basin salinity decorrelation scales. Asterisk indicates SNR values below 2.

Season	Depth (m)	Temporal (day)	Spatial (km)	SNR
Winter	Surface	30.1	201	5.69
	50	35.2	267	4.90
	100	—	—	—
Summer	Surface	23.2	230	3.00
	50	23.7	187	1.36*
	100	25.5	164	1.94*

c. Seasonal variabilities of the salinity decorrelation scales

Tables 6–8 present the salinity decorrelation scales and SNRs for JB, UB, and YB, respectively. The SNRs for salinity are smaller than the SNRs for temperature (Tables 3–5). This indicates that the salinity signal is weaker than the temperature signal in the JES. The larger noise might be caused by less salinity data (than temperature data) in MOODS.

The temporal and spatial decorrelation scales of salinity have weaker seasonal variability in comparison to the temperature field. The surface temporal decorrelation is shorter in summer than in winter (UB and YB, north of the Polar Front) and longer in summer than in winter (JB south of the Polar Front).

7. Observational network design

The temporal and horizontal decorrelation scales are useful for an optimal observational network design. The minimum sampling density required to detect thermohaline variabilities is two or three samples per decorrelation scale (e.g., Sprintall and Meyers 1991). Since the decorrelation scales of individual basin (JB, UB, YB) temperature and salinity fields have seasonal and vertical variabilities, the network design for the JES thermohaline observations should take this into account. For example, in the JB, surface temperature (salinity) measurements should be conducted at 81 km (66 km) and 7–8 day (12 day) intervals in the winter and at 155 km (57 km) and 5–6 day (8–9 day) intervals in the summer. These values are easily obtained from Tables 3–8.

8. Conclusions

1) Autocorrelation functions were constructed from 93 810 temperature and 50 349 salinity profiles (1930–97) on the Japan/East Sea from the U.S. Navy's Master Oceanographic Observational Data Set. The temporal and spatial decorrelation scales and their seasonal and vertical variations for the three major basins—Japan Basin, Ulleung Basin, and Japan Basin—were obtained. These scales associated with relatively large signal-to-noise ratio can be used for observational network design and observational data mapping.
2) The signal-to-noise ratios of temperature and salinity for both winter and summer are usually larger than 2. This indicates that both temperature and salinity signals in the Japan/East Sea are comparable to the Yellow Sea waters (Chu et al. 1997b). The signal-to-noise ratio is larger for temperature than for salinity, which might be caused by fewer salinity than temperature observations. The signal-to-noise ratios of temperature and salinity are greater in the summer than in the winter.
3) The seasonal variation in the autocorrelation functions of temperature at the surface is similar in the three basins: larger temporal and less spatial variability in summer than in winter. The temporal decorrelation scale is shorter in summer than in winter. Such strong seasonal variability at the surface is likely caused by the seasonal variability of the net surface heat flux.
4) Different ranges of the seasonal variation are found in the autocorrelation functions of temperature at the surface among the three basins: the maximum range in the Yamato Basin, the medium range in the Japan Basin, and the minimum range in the Ulleung Basin. The temporal decorrelation scale changes from 14.7 days in the summer to 30.5 days in the winter (15.8-day range) in the Yamato Basin, from 16.0 days in the summer to 23.0 days in the winter (7-day range)

TABLE 8. Seasonal and vertical variations of the Yamato Basin salinity decorrelation scales.

Season	Depth (m)	Temporal (day)	Spatial (km)	SNR
Winter	Surface	27.7	169	3.18
	50	34.4	189	4.90
	100	32.8	179	3.64
	200	—	—	—
Summer	Surface	30.5	238	2.59
	50	23.8	193	2.38
	100	23.3	162	4.90
	200	37.1	235	3.00

in the Japan Basin, and from 18.1 days in the summer to 23.8 days in the winter (5.7-day range) in the Ulleung Basin. The spatial decorrelation scale changes from 963 km in the summer to 309 km in the winter (654-km range) in the Yamato Basin, from 464 km in the summer to 242 km in the winter (222 km range) in the Japan Basin, and from 307 km in the summer to 251 km in the winter (56-km range) in the Ulleung Basin.

5) Among the three basins, the spatial thermal variability is weakest in the Yamato Basin (spatial decorrelation scale ranging from 309 to 963 km) for all seasons, strongest in the Ulleung Basin in the summer (spatial decorrelation scale around 307 km), and strongest in the Japan Basin in the winter (spatial decorrelation scale around 242 km). In the winter, the temporal thermal variability is weaker in the Yamato Basin (temporal decorrelation scale around 30.5 days) than in the Japan and Ulleung Basins (temporal decorrelation scale around 23–24 days). In the summer, the temporal thermal variability is weaker in the Ulleung Basin (temporal decorrelation scale around 18.1 days) than in the Japan Basin (16 days) and Yamato Basins (14.7 days).
6) The autocorrelation functions of salinity for the three basins have weaker seasonal variability in comparison to that of the temperature field. The surface temporal decorrelation has different seasonal variations among the three basins: shorter in summer (23.2 days in Ulleung Basin and 16.0 days in Japan Basin) and longer in winter (30.1 days in Ulleung Basin and 23.0 days in Japan Basin), except in the Yamato Basin, where it is longer in the summer (30.5 days) and shorter in the winter (27.7 days). The surface spatial decorrelation scales are 173 (197), 230 (201), and 238 (169) km in the Japan, Ulleung, and Yamato Basins during the summer (winter).
7) In the Japan Basin, high spatial coherence is found in the deep layer (300 m) for temperature and salinity, consistent with the concept of JES Proper Water proposed by Moriyasu (1972). In the Yamato Basin, high spatial coherence of salinity is found at depth 200 m in the summer.
8) The temporal and horizontal decorrelation scales are useful for designing an optimal observational network. Since the decorrelation scales of the temperature and salinity fields have an evident layered characteristics (larger values in the upper layer and smaller values in the intermediate layer), we should use different sampling densities. The minimum sampling density to detect temperature and salinity variabilities (one-third of the decorrelation scales) for each basin can be obtained from Tables 3–8.

Acknowledgments. The authors are grateful to Lynne Talley (the editor) for suggestions and two anonymous reviewers for comments on the preliminary draft. This work was funded by the Naval Oceanographic Office, the Office of Naval Research, and the Naval Postgraduate School, Wang Guihua also wishes to acknowledge the support by the key project, No. G1999043805, from China.

APPENDIX A

ACF Estimation

The ACF value for each bin (τ, r) is estimated by

$$\eta^{(z)}(\tau, r) = \frac{\sum_{\text{bin}(\tau,r)} \psi_o^{(z)\prime} \hat{\psi}_o^{(z)\prime}}{\sum_{\text{bin}(\tau,r)} [\psi_o^{(z)\prime}]^2}, \tag{A1}$$

which varies with the spatial and temporal lags (τ, r) and depth z. Whether the computed $\eta^{(z)}(\tau, r)$ is statistically significant should be tested by

$$\eta_\alpha^{(z)}(\tau, r) \equiv \frac{t_\alpha}{\sqrt{P^{(z)}(\tau, r) - 2 + t_\alpha^2}} \tag{A2}$$

with the significance level of α and the t distribution of $[P^{(z)}(\tau, r) - 2]$ degrees of freedom (Chu et al. 1997b). When $\eta^{(z)}(\tau, r) > \eta_\alpha$, the estimated ACF is significant on the level of α. Since both $\eta^{(z)}(\tau, r)$ and $\eta_\alpha^{(z)}(\tau, r)$ have seasonal variations, the significance of the ACF estimation should also change with seasons. Significant ACF estimation ($\alpha = 0.10$) is limited to the areas on the (τ, r) plane with positive values of

$$\Delta\eta = \eta^{(z)}(\tau, r) - \eta_\alpha^{(z)}(\tau, r) \tag{A3}$$

and is not significant for areas with negative values.

APPENDIX B

Signal-to-Noise Ratio (SNR)

The measured variance s^2 of the thermal fields is separated into signal and noise, whereby

$$s^2 = s_s^2 + s_n^2.$$

The noise variance has two sources, geophysical and instrumentation errors. Here, the geophysical error is unresolved thermal variability with scales smaller than the typical time and space scales between two temperature profiles. In this study the unresolved scales are 0.5 day and 5 km. The ACF value in the first bin (0, 0) does not represent the correlation between profiles paired by themselves, and therefore does not equal 1. Following Sprintall and Meyers (1991) the signal-to-noise ratio is computed by

$$\lambda \equiv \frac{s_s}{s_n} = \sqrt{\frac{\eta(0, 0)}{1 - \eta(0, 0)}}. \tag{B1}$$

The larger the λ, the smaller the geophysical error. If $\eta(0, 0) = 1$, there is no noise and $\lambda = \infty$. If $\eta(0, 0) = 0$, there is no signal. If $\lambda > 2$, the ratio of the signal

variance, s_s^2, to the noise variance, s_n^2, is greater than 4, which was considered quite good by White et al. (1982) and Sprintall and Meyers (1991).

REFERENCES

Chu, P. C., 1995: P-vector method for determining absolute velocity from hydrographic data. *Mar. Technol. Soc. J.,* **29** (3), 3–14.

——, H.-C. Tseng, C. P. Chang, and J. M. Chen, 1997a: South China Sea warm pool detected in spring from the Navy's Master Oceanographic Observational Data Set (MOODS). *J. Geophys. Res.,* **102,** 15 761–15 771.

——, S. K. Wells, S. D. Haeger, C. Szczechowski, and M. Carron, 1997b: Temporal and spatial scales of the Yellow Sea thermal variability. *J. Geophys. Res.,* **102,** 5655–5668.

——, Y. C. Chen, and S. H. Lu, 1998: Temporal and spatial variabilities of Japan Sea surface temperature and atmospheric forcing. *J. Oceanogr.,* **54,** 273–284.

——, J. Lan, and C. W. Fan, 2001a: Japan/East Sea circulation and thermohaline structure. Part II: A variational P-vector method. *J. Phys. Oceanogr.,* **31,** 2886–2902.

——, ——, and ——, 2001b: Japan Sea circulation and thermohaline structure. Part I: Climatology. *J. Phys. Oceanogr.,* **31,** 244–271.

Clancy, R. M., 1983: The effect of observational error correlations on objective analysis of ocean thermal structure. *Deep-Sea Res.,* **30,** 985–1002.

Hase, H., J.-H. Yoon, and W. Koterayama, 1999: The current structure of the Tsushima Warm Current along the Japanese coast. *J. Oceanogr.,* **55,** 217–235.

Hong, C. H., K. D. Cho, and S. K. Yang, 1984: On the abnormal cooling phenomenon in the coastal areas of East Sea of Korea in the summer 1981. *J. Oceanol. Soc. Korea,* **19,** 11–17.

Isoda, Y., and S. Saitoh, 1988: Variability of the sea surface temperature obtained by the statistical analysis of AVHRR imagery—A case study of the south Japan Sea. *J. Oceanogr. Soc. Japan,* **44,** 52–59.

——, and ——, 1993: The northward intruding eddy along the east coast of Korea. *J. Oceanogr.,* **49,** 443–458.

Kano, Y., 1980: The annual variation of the temperature, salinity and oxygen contents in the Japan Sea. *Oceanogr. Mag.,* **31,** 15–26.

Kawabe, M., 1982a: Branching of the Tsushima Current in the Japan Sea, Part I: Data analysis. *J. Oceanogr. Soc. Japan,* **38,** 95–107.

——, 1982b: Branching of the Tsushima Current in the Japan Sea, Part II: Numerical experiment. *J. Oceanogr. Soc. Japan,* **38,** 183–192.

Kim, K., and J. Y. Chung, 1984: On the salinity-minimum and dissolved oxygen-maximum layer in the East Sea (Sea of Japan). *Ocean Hydrodynamics of the Japan and East China Seas,* T. Ichiye, Ed., Elsevier Science, 55–65.

——, Y.-G. Kim, Y.-K. Cho, M. Takematsu, and Y. Volkov, 1999: Basin-to-basin and year-to-year variation of temperature and salinity characteristics in the East Sea (Sea of Japan). *J. Oceanogr.,* **55,** 103–109.

Kim, Y.-G., and K. Kim, 1999: Intermediate Waters in the East/Japan Sea. *J. Oceanogr.,* **55,** 123–132.

Maizuru Marine Observatory, 1997: Climate chart of the Japan Sea. Maizuru, Japan.

Martin, S., and M. Kawase, 1998: The southern flux of sea ice in the Tatarskiy Strait, Japan Sea and the generation of the Liman Current. *J. Mar. Res.,* **56,** 141–155.

Miyazaki, M., 1953: On the water masses of the Japan Sea (in Japanese with English abstract). *Bull. Hokkaido Reg. Fish. Res. Lab.,* **7,** 1–65.

Moriyasu, S., 1972: The Tsushima current. *Kuroshio, Its Physical Aspects,* H. M. Stommel and K. Yoshida, Eds., University of Tokyo Press, 353–369.

Phoebus, P. A., 1988: Improvements to the data selection algorithms in the Optimum Thermal Interpolation System (OTIS). Naval Ocean Research and Development Activity Rep. 239, 18 pp.

Senjyu, T., 1999: The Japan Sea Intermediate Water: Its characteristics and circulation. *J. Oceanogr.,* **55,** 111–122.

Seung, Y.-H., 1994: The separation of the East Korean Warm Current and the mechanism for the formation of the North Korean Cold Current (in Japanese). *Kaiyo Mon.,* **9,** 758–765.

Slutz, R. J., S. J. Lubker, J. D. Hiscox, S. D. Woodruff, R. L. Jenne, D. H. Joseph, P. M. Steurer, and J. D. Elms, 1985: Comprehensive Ocean–Atmosphere Data Set. CIRES/ERL/NCAR/NCDC, 268 pp.

Sprintall, J., and G. Meyers, 1991: An optimal XBT sampling network for the eastern Pacific Ocean. *J. Geophys. Res.,* **96,** 10 539–10 552.

Teague, W. J., M. J. Carron, and P. J. Hogan, 1990: A comparison between the Generalized Digital Environmental Model and Levitus climatologies. *J. Geophys. Res.,* **95,** 7167–7183.

Uda, M., 1934: The results of simultaneous oceanographic investigations in the Japan Sea and its adjacent waters in May and June, 1932 (in Japanese). *J. Imp. Fish. Exp. Stn.,* **5,** 57–190.

White, W. B., G. Meyers, and K. Hasunuma, 1982: Space/time statistics of short-term climatic variability in the western North Pacific. *J. Geophys. Res.,* **87,** 1979–1989.

Yoon, J.-H., 1982: Numerical experiment on the circulation in the Japan Sea, Part I. Formation of the East Korean Warm Current. *J. Oceanogr. Soc. Japan,* **38,** 43–51.